Influence of the modification of iron-bearing intermetallic and eutectic Si on the mechanical behavior near the solidus temperature in Al-Si-Cu 319 cast alloy

Kun Liu *, X. Grant Chen

University of Quebec at Chicoutimi, QC, Canada, G7H 2B1

(* Corresponding author: kun.liu@uqac.ca; Tel.:1-4185455011 ext. 7112; Fax: 1-4185455012)

Abstract

The mechanical behavior near the solidus temperature in Al-Si-Cu 319 cast alloys was studied in both the solid and semisolid states. Mn and Sr were introduced to modify the iron-bearing intermetallic from platelet β-Fe to Chinese script α-Fe and the eutectic Si particles from a flake to fibrous shape, respectively. During the high-temperature tensile tests, the strength and ductility of the alloys decreased with increasing temperature and liquid fraction. The mechanical behavior at a given temperature near the solidus was mainly controlled by iron-bearing intermetallics and eutectic Si particles. In both the solid and semisolid states, the high-temperature mechanical properties are improved due to the modification of the iron-bearing intermetallics from platelet β-Fe to Chinese script α-Fe by Mn addition, while they are further enhanced by the simultaneous modification of the iron-bearing intermetallics and eutectic Si particles by the combined additions of Mn and Sr. The fracture surfaces of the tensile samples under solid and semisolid conditions were examined to study the crack initiation and propagation. The susceptibility to hot tearing for the alloys with different microstructures is discussed.

Keywords: Al-Si-Cu 319 cast alloy; High-temperature mechanical properties; Iron-bearing intermetallic; Eutectic Si.

1. Introduction

Due to their excellent mechanical properties and castability, Al-Si-Cu cast alloys have been widely used in automotive applications, such as for engine cylinder heads and engine blocks [1, 2]. During the casting process, casting defects, such as hot cracks, hot tearing and porosity, can often arise due to the high tensile stress/strain from the thermal gradients and solidification shrinkage in temperatures near the solidus, which are very detrimental to material properties and product quality [3-6]. Therefore, understanding the allowable tensile strain/stress near the solidus temperature in both the solid and semisolid states is the key to further discover the root cause of such casting defects.

To study the mechanical properties of a material near the solidus temperature, three types of mechanical tests are often used: compression [7-9], shear [9, 10], and tension [4-6, 11-14]. Among these tests, the high-temperature tensile test is widely accepted to produce a similar stress-strain condition to what the material experienced during solidification [13, 14]. Several studies have performed the high-temperature tensile testing on different aluminum alloys and obtained significant findings for high-temperature mechanical properties of the alloys. For instance, Bolouri *et al.* [5] performed the tensile tests near the solidus temperature in Al-Cu 206 cast alloy by directly heating the sample in a Gleeble thermal-mechanical simulator and found that the addition of grain refiner could decrease the sensitivity of hot tearing. Phillion *et al.* [13] also measured the tensile properties above the solidus temperature in AA 6111 and CA31218 aluminum alloy and reported that the critical solid fraction to the complete loss of ductility was greatly dependent on alloys, which was ~ 0.99 for AA 6111 but ~ 0.94 for CA31218. However, limited knowledge on the high-temperature mechanical properties near the solidus temperature of Al-Si-Cu cast alloys exists. It is one of key concerns to further understanding the castability and casting quality for their industrial applications.

Al-Si-Cu 319 alloy is one of the most widely used cast alloys due to its good combination of properties at room temperature and elevated temperature [1]. Generally, 319 alloys are secondary cast alloys, in which the iron content can reach a level high enough to form the various iron-bearing intermetallics [2]. It has been reported that platelet β-Al_5FeSi (coded as β-Fe) is the most observed iron-bearing intermetallic in 319 alloys, which is very detrimental to the mechanical properties due to its platelet

morphology leading to a stress concentration and crack initiation [15, 16]. In addition, the formation of the platelet β-Fe intermetallic could increase the porosity content and hot-tearing sensitivity through a variety of mechanisms, including blocking of interdendritic flow, acting as the nuclei and helping the growth of pores [17-20]. Therefore, neutralization elements, such as Mn, are often added to modify the platelet β-Fe to Chinese script α-$Al_{15}(FeMn)_3Si_2$ (coded as α-Fe) to improve the room-temperature mechanical properties [21-23]. The other most significant microstructure in 319 alloys is eutectic Si [24, 25]. Without modification, the Si particles have a flake-like morphology, which is reported to be deleterious to the alloy properties, especially on the elongation [25]. Hence, the flake-like Si particles are generally modified into fine fibrous particles through Sr, Na and rare earth elements to improve the mechanical properties [24, 26, 27]. However, little work has been performed about the influence of modification of iron-bearing intermetallics and eutectic Si on the high-temperature properties, particularly near the solidus temperature.

In the present work, the high-temperature tensile properties (slightly below and above the solidus temperature) of Al-Si-Cu 319 cast alloys with the additions of Mn and Sr were investigated using a Gleeble 3800 thermal-mechanical simulator. The evolution of the microstructure and fracture surfaces was characterized, and the role of iron-bearing intermetallics and Si particles in the high-temperature properties are discussed.

2. Experimental process

2.1 Alloy preparation

Three experimental 319 alloys were prepared with commercially pure Al (99.7%) and pure Mg (99.9%), Al-50% Cu, Al-25% Fe, Al-50% Si and Al-25% Mn, and Al-10% Sr master alloys. Among these three alloys, Alloy A was designed as the base alloy, in which the principal iron-bearing intermetallic is platelet-like β-Fe, whereas the intermetallic was modified into Chinese script α-Fe by the addition of Mn in Alloy B. However, the eutectic Si particles are still flake-like in both Alloys A and B [21]. Alloy C was prepared with the additions of Mn and Sr to modify both the intermetallics and eutectic Si [25]. Their chemical compositions were analyzed by optical emission spectrometry and are shown in Table 1.

Table 1 Chemical compositions used in present work

Alloy Code	Element (wt. %)					
	Si	Cu	Mg	Fe	Mn	Sr
Alloy A	5.54	3.16	0.18	0.22	0	0
Alloy B	5.98	3.26	0.11	0.23	**0.22**	0
Alloy C	5.73	3.09	0.12	0.28	**0.23**	**0.0098**

In each test, approximately 30 kg of materials was melted in a clay-graphite crucible using an electric resistance furnace. The melt was held at 750 °C for 30 minutes and degassed for 15 minutes using pure argon. Finally, the melt was poured into a standard ASTM B-108 permanent mold that was preheated at 450 °C to obtain the tensile bars.

2.2 High-temperature tensile tests

The high-temperature tensile tests were performed with a Gleeble 3800 thermal-mechanical simulator. The cylindrical specimens with a total length of 120 mm and a diameter of 10 mm were machined from the standard ASTM B108 tensile bars (Fig. 1). During the tests, the specimen was loaded in the horizontal orientation and held by two grips. The specimen was heated directly via electro-resistance heating. The specimen was first heated to 450 °C at a heating rate of 2 °C/s and then held for 45 seconds. Subsequently, the specimen was heated to 5 - 7 °C below the target temperature at a heating rate of 2 °C/s. A further increase to the target temperature was manually performed to avoid the overheating. For the tests in the semisolid state, a free movable ceramic tube is set on the specimen to avoid aluminum liquid leakage at the end of tensile deformation (Fig. 1). Such a temperature-control approach and the setup of the tensile specimen can guarantee that the temperature profiles were symmetric and that the maximum temperature variation was approximately 1 °C in the middle zone (5 – 6 mm) of the specimen. Details can be found in our previous work [5]. A minimum of three tests was conducted at each condition with a strain rate of 0.001/s. The data acquisition rate was 200/sec to obtain the sufficient data. The stresses measured in the present work are engineering stresses and their values (σ) are calculated as $\sigma = \frac{F}{A_0}$, in which F is the force and A_0 is the cross-section area of specimen before deformation.

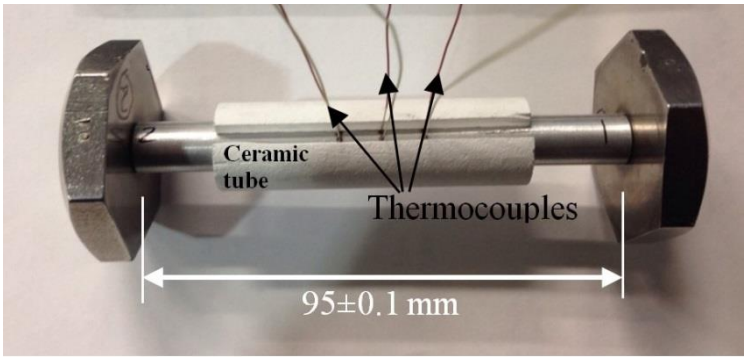

Fig. 1 Specimen used for high-temperature tensile test in the present work

For the tests in the semisolid state, the solidus temperature and the liquid fraction as a function of temperature were determined by a differential scanning calorimeter (DSC). The DSC heating curves were used to calculate the liquid fraction vs. temperature according to the literature [28]. The heating rate of the DSC curves was set at 10 °C/min. The calculated liquid fraction vs. temperature for experimental alloys is shown in Fig. 2. In addition, the solidus temperatures and the corresponding temperatures to various liquid fractions applied in the present work are summarized in the insert table of Fig. 2.

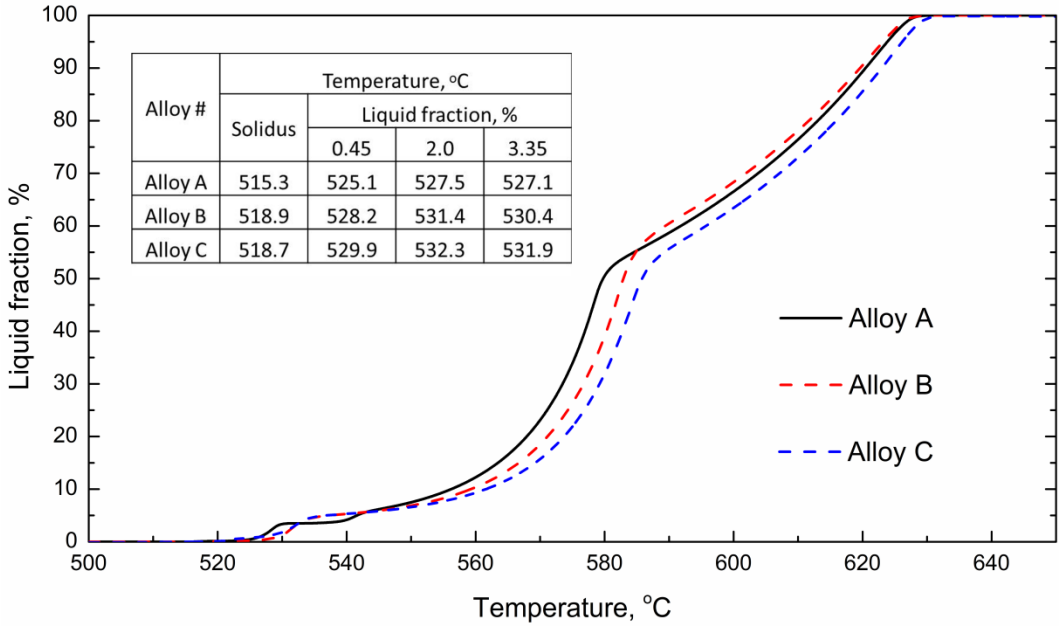

Alloy #	Temperature, °C			
	Solidus	Liquid fraction, %		
		0.45	2.0	3.35
Alloy A	515.3	525.1	527.5	527.1
Alloy B	518.9	528.2	531.4	530.4
Alloy C	518.7	529.9	532.3	531.9

Fig. 2 Liquid fraction vs temperature calculated from DSC curves of experimental alloys

2.3 Microstructure characterization

An optical microscope (OM) and scanning electron microscope (SEM) equipped with energy-dispersive X-ray spectroscopy (EDS) were used to characterize the microstructure of the as-cast samples and fracture surface after the tensile test. In addition, the cross-sections parallel to the loading direction of the tensile samples before failure were also prepared and observed using OM and SEM to observe the initiation and growth of the crack during the tensile tests.

3. Results and Discussion

3.1 Microstructure of experimental alloys

Fig. 3 shows the as-cast microstructure of three experimental alloys. Generally, the microstructure of the three alloys is composed of Al dendrites, θ-Al_2Cu, eutectic Si and iron-bearing intermetallics. However, the morphology of the iron-bearing intermetallics and Si particles varies with alloy composition. In Alloy A, the dominant iron-bearing intermetallic is the platelet-like β-Fe, while the Si particles are flake-like (Fig. 3a). With the addition of Mn into Alloy B, the platelet-like β-Fe was modified into Chinese script α-Fe, but the Si particles are still flake-like (Fig. 3b). With the combined additions of Mn and Sr in Alloy C (Fig. 3c), the flake-like Si particles have been modified into fine fibrous particles, but the dominant intermetallic is still Chinese script α-Fe. The modifications of the iron-bearing intermetallics and Si particles in the experimental alloys are in agreement with the literature [21, 24, 25]. Besides, the secondary dendrite arm space (SDAS) is measured to be similar for all three alloys, which is 20-25 μm.

Table 2 shows the characterization results of the eutectic Si and dominant iron-bearing intermetallics from image analysis. The length of the particle in the table is referred to as the maximum length from all the directions of particles. It can be seen that the area percentage of the Si particles is similar in the experimental alloys, which is approximately 7%. However, the average length is remarkably different for the alloys and is much higher in Alloys A and B (~ 16 μm) than in Alloy C (~ 2 μm). This is greatly related to the modification of the Si particles. For the dominant iron-bearing intermetallics, the area percentage of β-Fe in Alloy A is 3%, whereas it increases to approximately 4% in Alloys B and C with dominant α-Fe. Due to the change in the

morphology, the average length of the intermetallics changed from 12.5 μm for the platelet β-Fe in Alloy A to 5.3 μm and further to 3.5 μm for the Chinese script α-Fe in Alloy B and Alloy C, respectively.

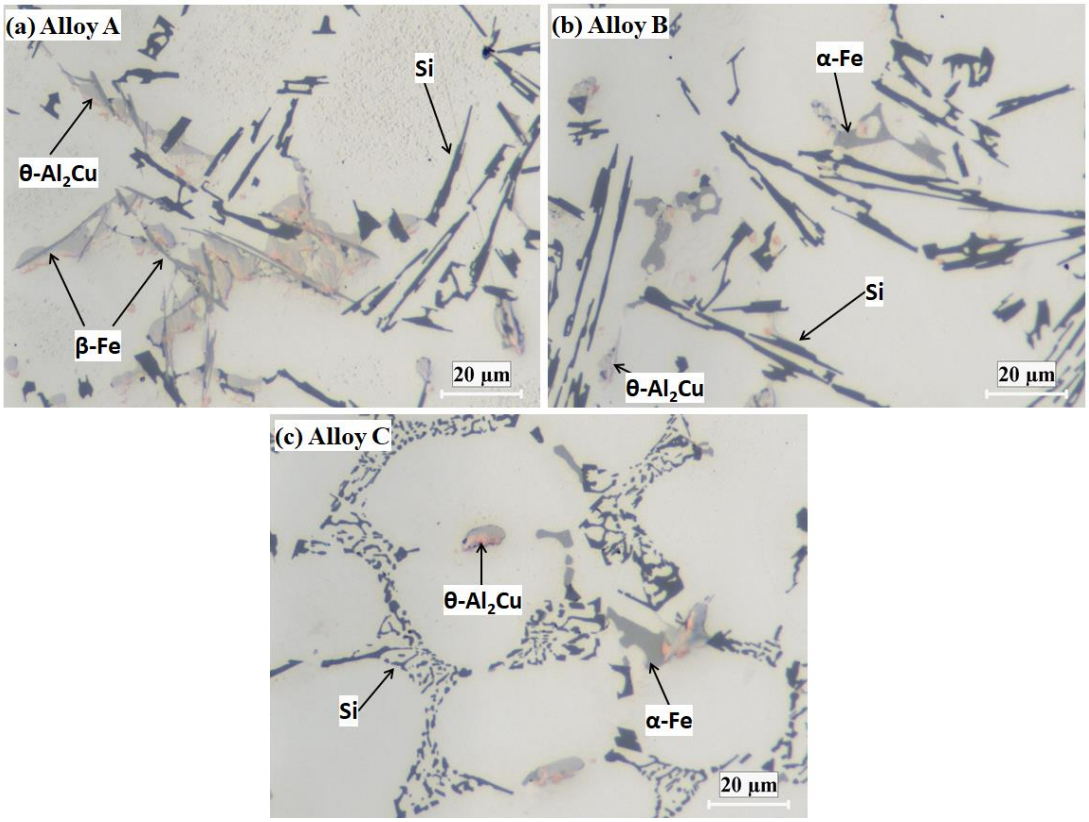

Fig. 3 As-cast microstructure of experimental alloys

Table 2 Characterization of Si and dominant iron-bearing intermetallic

Alloy	Eutectic Si		Iron-bearing intermetallic	
	Area percentage，%	Average Length, μm	Area percentage，%	Average Length，μm
Alloy A	7.22	16.3	3.01	12.5
Alloy B	6.98	14.2	4.32	5.3
Alloy C	6.77	2.2	4.19	3.5

3.2 Mechanical behavior in the solid state

As shown in Fig. 2, the solidus temperature of Alloy A is approximately 515 °C, which is slightly lower than that of Alloy B (519 °C). Therefore, the temperature range for the tensile tests in the solid state was selected from 460 to 510 °C to ensure that the alloys are in the solid state. The tensile stress-displacement curves of the experimental alloys are shown in Fig. 4. In the present work, the displacement but not strain was used because the length change of the deformed zone during testing is not precisely known.

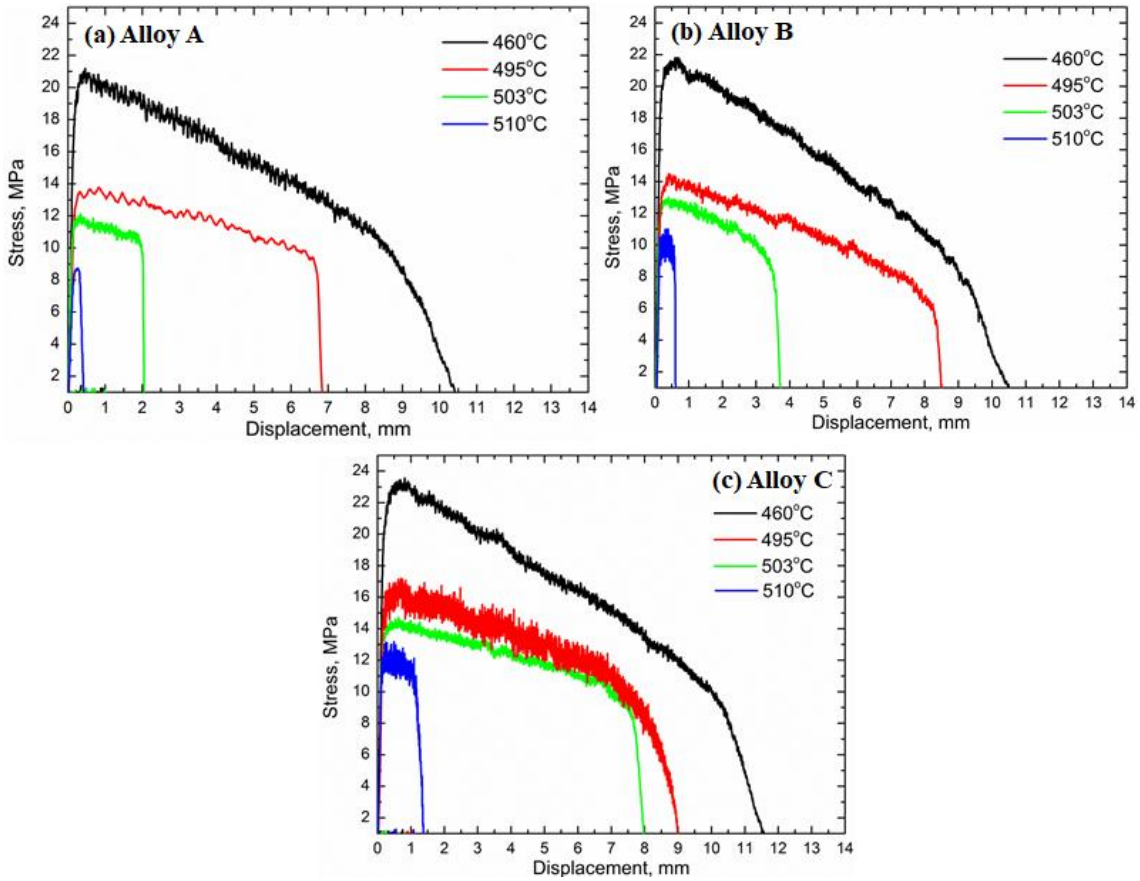

Fig. 4 Typical stress-displacement curves at various temperatures of experimental alloys

As shown in Fig. 4, the general tendency for experimental alloys is that the maximum stress decreases with increasing temperature. For instance, the maximum stress decreases from 21.1 MPa at 460 °C to 13.1 MPa at 495 °C and further to 8.8 MPa at 510 °C for Alloy A. The decrease of the maximum stress can be attributed to the facilitated dislocation/grain boundary movement at higher temperatures [12, 29-32]. It is known that the movement of dislocations through a lattice is accomplished by thermal variations, which are strongly related to temperature. As the temperature increases, the

potential for dislocation climb and slip increases, leading to a decreasing resistance to dislocation movement, especially at the temperatures near the solidus used in the present work. In addition, the grain boundary slip becomes easier at higher temperatures. It is reported that the work softening in Al-Si-Cu 319 alloys becomes increasingly effective at temperatures higher than 270 °C [12]. Therefore, the maximum stress of the experimental alloys shows a decreasing tendency with increasing temperature under the mechanism of combined movement of dislocations and grain boundaries.

On the other hand, the displacement at failure also decreases with increasing temperature. For instance, the displacement in Alloy A is 10.4 mm at 460 °C and decreases to 6.8 mm at 495 °C and even to 0.38 mm at 510 °C. It is interesting to note that there is a sharp decrease in the ductility at temperatures close to the solidus from 495 to 510 °C. The displacement at failure is greatly reduced from a relatively high level below 495 °C to a very low level at 510 °C. For example, the displacement in Alloy A is 6.8 mm at 495 °C, but it sharply decreases to 0.38 mm at 510 °C, while it decreases from 8.5 and 9.1 mm at 495 °C to 0.66 and 1.34 mm at 510 °C in Alloys B and C, respectively. This can be principally attributed to the more openings in the intergranular region away from the fracture surface at high temperatures close to the solidus temperature [14].

The trends for the maximum stress and displacement vs. temperature can be clearly illustrated in Fig. 5. Compared with Alloy A, both the maximum stress and displacement increase with the addition of Mn in Alloy B and further increase with the combined additions of Mn and Sr in Alloy C at all temperatures studied. For instance, when tested at 503 °C, the maximum stress increases from 11.7 MPa in Alloy A to 13.1 MPa in Alloy B and further to 14.7 MPa in Alloy C, whereas the displacement increases from 2 mm in Alloy A to 3.7 mm in Alloy B and further to 8 mm in Alloy C. It is evident that the improvement of the tensile strength and ductility is greater in Alloy C than in Alloy B relative to the base alloy (Alloy A).

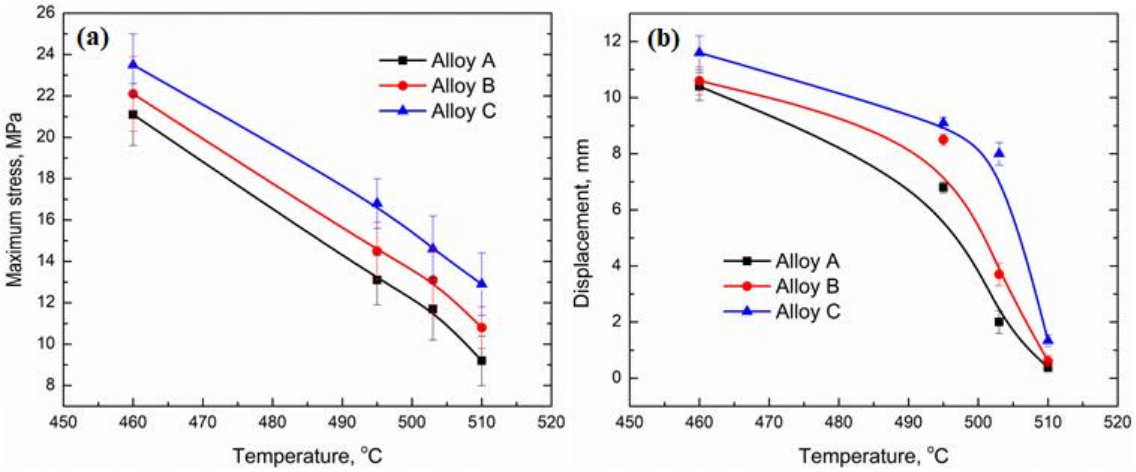

Fig. 5 Evolution of maximum stress and failure displacement with testing temperature

The cross-sections parallel to the loading direction of the fractured areas in the three alloys after testing at 503 °C are shown in Fig. 6. In Alloy A (Fig. 6a and b), the branches of the platelet-like β-Fe and flake-like Si are frequently observed along the propagation path of the principal and secondary cracks. Fig. 6b also clearly shows that the cracks can rapidly propagate along the branches of the flake-like Si. In materials that are subjected to monotonic tensile stress, the fracture begins with the initiation of cracks followed by their propagation. The release of stresses that are carried by the secondary particles, such as iron-bearing intermetallics and Si, will affect the overall load bearing capacity of the materials. Therefore, the platelet β-Fe and flake-like Si particles in Alloy A easily become the sites for crack initiation and channels for crack propagation due to local stress concentration [25, 33], resulting in the low strength and ductility (Fig. 5).

However, in Alloy B with Mn, where the platelet-like β-Fe was modified to the Chinese script α-Fe (Fig. 3b), only the branches of the flake-like Si particles are frequently observed in the fracture cross-section, whereas the Chinese script α-Fe blocks the crack propagation (Fig. 6c). With further addition of Sr in Alloy C, the flake-like Si particles are modified into fine fibrous particles (Fig. 3c), which leads to crack propagation difficulties along the fine Si branches (Fig. 6d) and then results in the highest strength and ductility among the three alloys (Fig. 5). The greater improvement in the tensile properties in Alloy C compared to the improvement in those of Alloy B is attributed to Alloy C having a higher area percentage of Si particles than intermetallics.

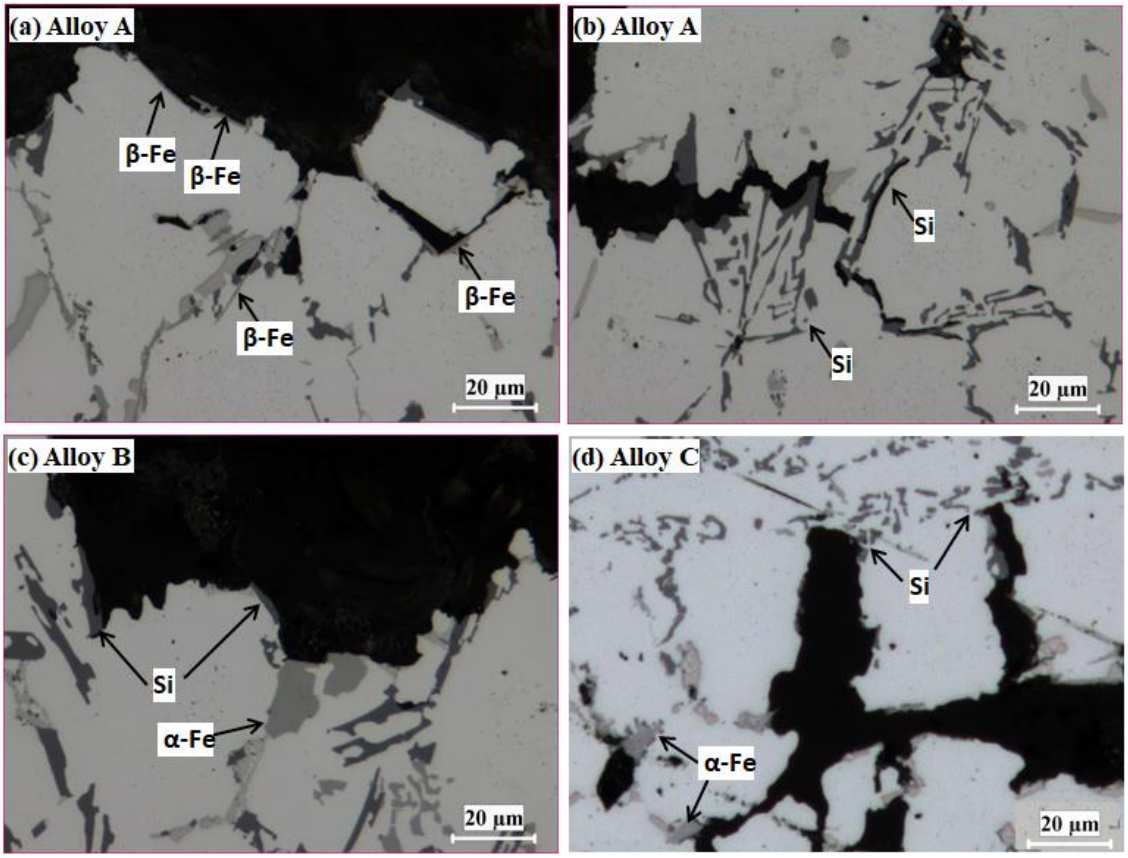

Fig. 6 Cross-section of fractures of three experimental alloys

Fig. 7 shows the fracture surfaces of Alloys A and C after testing at 503 °C. In Alloy A (Fig. 7a), the large platelets of β-Fe and branches in the Si flakes can be obviously observed on the fracture surface, whereas no dimples are present in this alloy, indicating brittle fracture and low ductility for Alloy A. However, a number of dimples can be observed in Alloy C (Fig. 7b) with fine Si fibers and α-Fe particles on the fracture surface, showing a more ductile fracture [34], confirming the high strength and ductility of Alloy C in Fig. 5. Note that the particles in Alloy C (Fig. 7b), such as the Si fibers and Chinese script α-Fe, were shattered into multiple pieces due to the increasing stress accumulation at the matrix/particle interfaces [12, 30]. However, the platelet β-Fe and flake-like Si in Alloy A (Fig. 7a) more or less remained in their original morphology because the crack can easily propagate along their platelet direction and then release the accumulated stress.

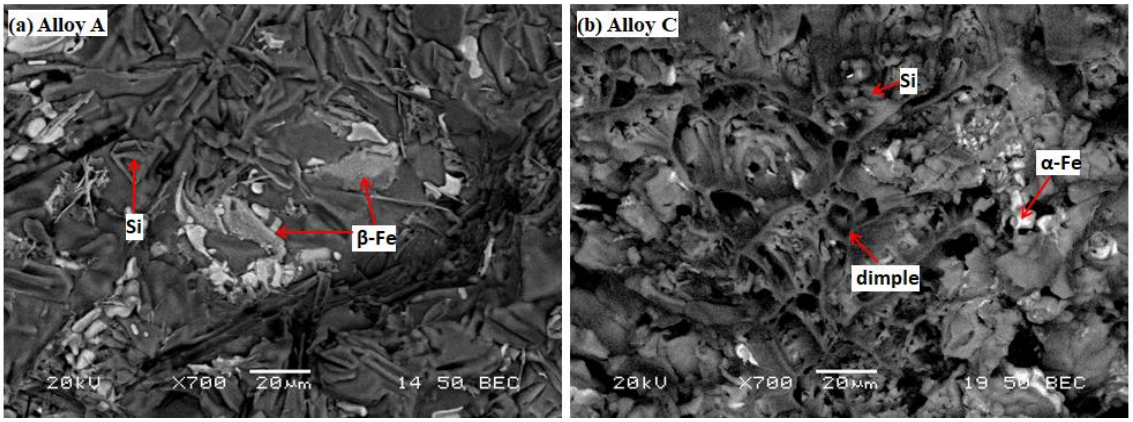

Fig. 7 Fracture surfaces of Alloy A (a) and Alloy C (b) after tensile testing at 503 °C

3.3 Mechanical behavior in semisolid state

For tensile tests in the semisolid state, slightly different temperatures were set to keep the same liquid fraction among the three experimental alloys according to Fig. 2. Three liquid fractions (0.45%, 2% and 3.35%) were selected, which are in the sensitive liquid fraction range (within 5%) for hot tearing [5]. The typical stress-displacement curves at 0.45% and 3.35% liquid fractions for the three experimental alloys are shown in Fig. 8. In general, the stress increases to reach the maximum level and then decreases toward zero. Tensile cracks can be assumed to initiate at the maximum stress. The low maximum stress and displacement of an alloy indicates that cracks can easily form. As shown in Fig. 8, the maximum stress and displacement are reduced from Alloy C to Alloy B and further to Alloy A.

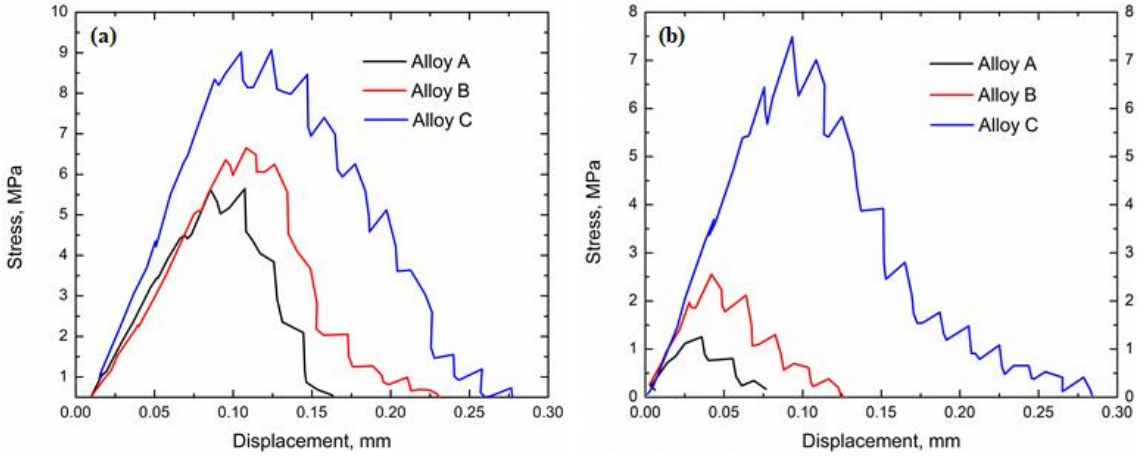

Fig. 8 Tensile stress-displacement curves at the liquid fraction of: (a) 0.45% and (b) 3.35%

The evolution of the maximum stress and displacement at failure during the semisolid tensile tests is shown in Fig. 9. At the low liquid fraction (0.45%), the three alloys still possess reasonably high values of stress and displacement, and their mechanical behavior is controlled by the solid skeleton. The material response is similar to that tested at a temperature close to solidus in the solid state (510 °C, see Fig. 5). With increasing liquid fraction, the maximum stress and displacement decrease remarkably, indicating that the mechanical behavior of the alloys is dependent on the liquid portion surrounded. For instance, the maximum stress decreases from 5.2 to 1.25 MPa in Alloy A as the liquid fraction increases from 0.45% to 3.35%, while the displacement decreases from 0.14 mm to an insignificant level (0.05 mm). It is clear that with such a low strength and ductility, Alloy A has a very low ability to accommodate strains during the last stage of solidification, which increases the possible occurrence of hot cracks. The trend for the stress and displacement development with liquid fraction is similar in Alloy B. However, the maximum stress and displacement in Alloy B are always higher than those of Alloy A at any given liquid fraction, showing the beneficial effect of the modification of the iron-bearing intermetallic from Mn addition on tensile properties at mush zone.

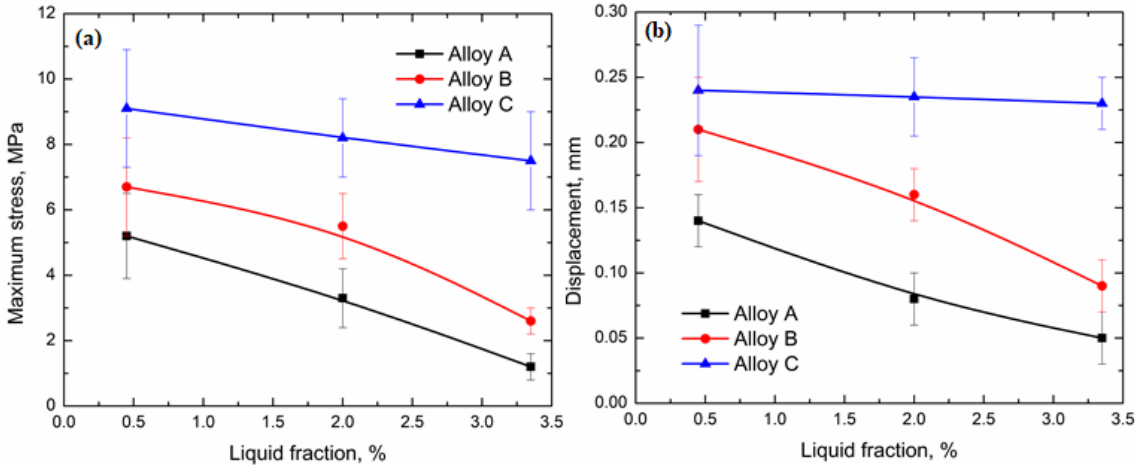

Fig. 9 Evolution of maximum stress and displacement at failure as a function of liquid fraction

As shown in Fig. 9, in Alloy C, the maximum stress decreases only slightly from 9.1 MPa 7.5 MPa as the liquid fraction creases at 3.35%, while the displacement remains almost unchanged at a relatively high level. Compared to those in Alloys A and B, Alloy C exhibits the highest strength and ductility within the experimental range of the liquid

fraction, and it can sustain more deformation before failure, resulting in the highest resistance to hot crack propagation. It is evident that the simultaneous modification of the iron-bearing intermetallic and eutectic Si particles by the combined additions of Mn and Sr in Alloy C can significantly improve the mechanical properties in the semisolid state. According to the literature [5], the aluminum alloy that has a higher strength and ductility at a given liquid fraction, especially in the sensitive liquid fraction range (within 5%) for hot tearing, is less prone to hot cracking than those with lower strength and ductility. Therefore, the susceptibility to hot tearing should decrease in the order of Alloy A, Alloy B and Alloy C, which is consistent with the literature [3, 35, 36].

To verify the role of the iron-bearing intermetallics and eutectic Si particles on the semisolid tensile properties, the observation of fracture surface in the experimental alloys at the liquid fraction of 3.35% was performed, and the results are shown in Fig. 10.

As shown in Fig. 10, it seems that all the fractures are intergranular and do not contain dimples, showing a relatively brittle behavior in comparison with the fracture in the solid state (Fig. 7). However, the differences in the fracture surface between the alloys can be observed. As shown in Fig. 10a, a few large pores are present in the fracture of Alloy A, which is likely due to the large platelet β-Fe that acts as an initiator of porosity [2], whereas fewer defects can be observed in Alloys B and C. In addition, the morphology of the fracture varies with alloys. In Alloy A (Fig. 10a-b), the fracture is intergranular with coarse granular morphology (Fig. 10b). However, a mixture of smooth intergranular and dendritic morphology is exhibited in Alloy B (Fig. 10c-d). As shown in Fig. 10d, the intergranular fracture is smoother than that in Fig. 10b, and the dendritic fracture (indicated by the red circle) is also present in Alloy B. In Alloy C, it is obvious that the fracture is almost dendritic (indicated by the red circle), and they are finer in Alloy C than that in Alloy B (Fig. 10e). It has been reported that the formation of coarse intergranular fractures is from the non-continuous and isolated liquid pockets in the interdendritic regions, while dendritic fractures are result from the movement of liquid around solid grains during deformation, which can possibly heal initiated cracks and delay the fracture [14, 37]. Therefore, the transition of less brittle/brittle fractures in the experimental alloys is closely related to the morphology of the eutectic Si particles and

iron-bearing intermetallics, which plays a significant role in the interaction between the solid grains and liquid films during the semisolid tensile tests.

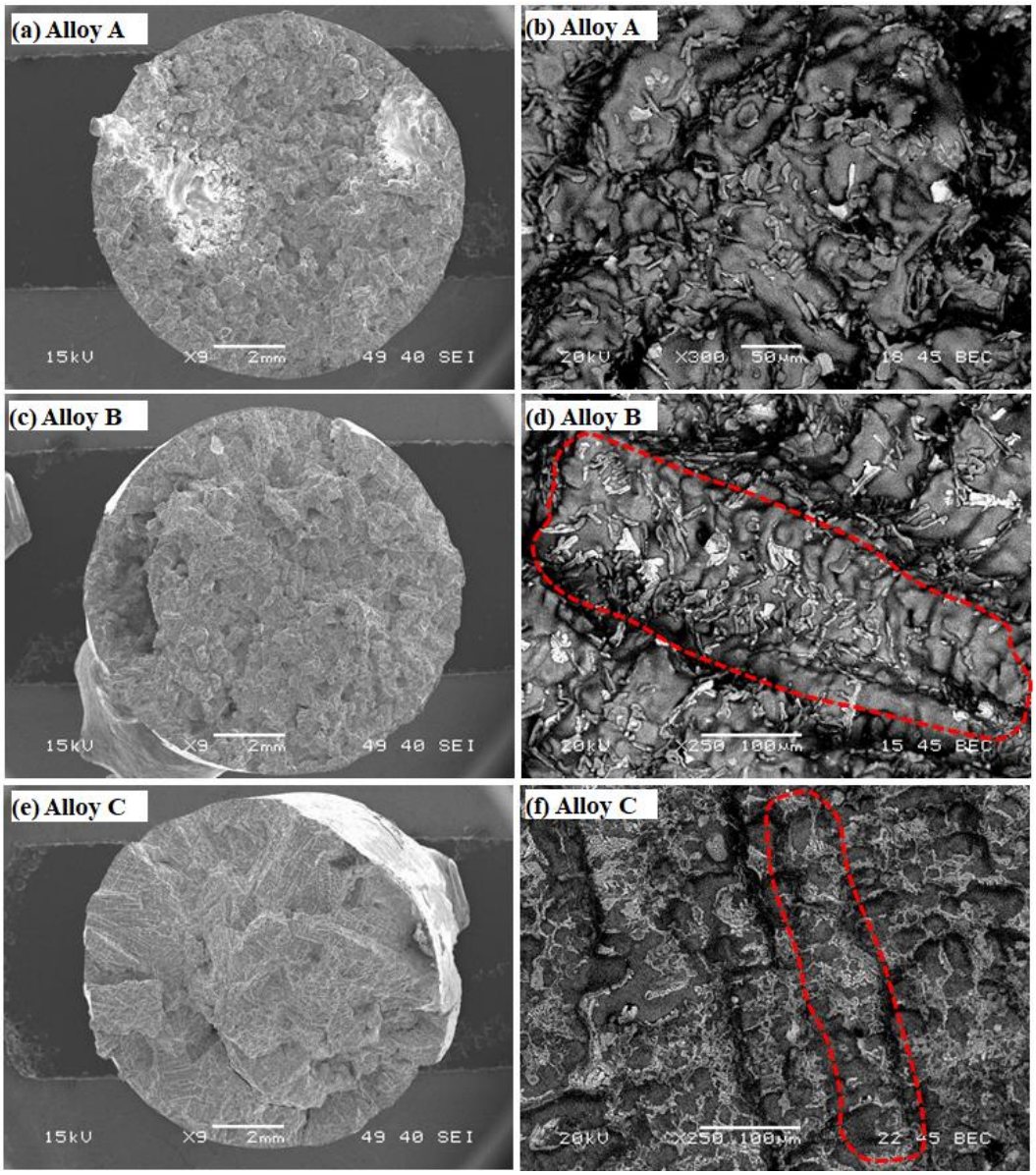

Fig. 10 Fractures after semi-solid tensile tests at the liquid fraction of 3.35%: (a-b) Alloy A, (c-d) Alloy B and (e-f) Alloy C

Fig. 11 shows the details of the fracture surfaces of the experimental alloys after testing at a liquid fraction of 3.35%. The compact Si particles and iron-bearing intermetallics can be observed on the fracture surfaces of all the experimental alloys, confirming the intergranular fracture nature during the semisolid tensile test. As shown in Fig. 3, Al_2Cu is always observed in the experimental alloy intersected with the Si and

iron-bearing intermetallics. It is known that eutectic Al_2Cu particles are the lowest melting point component compared with the eutectic Si and iron-bearing intermetallics. Therefore, eutectic Al-Al_2Cu remelts first above the solidus in the interdendritic area during the semisolid tensile tests.

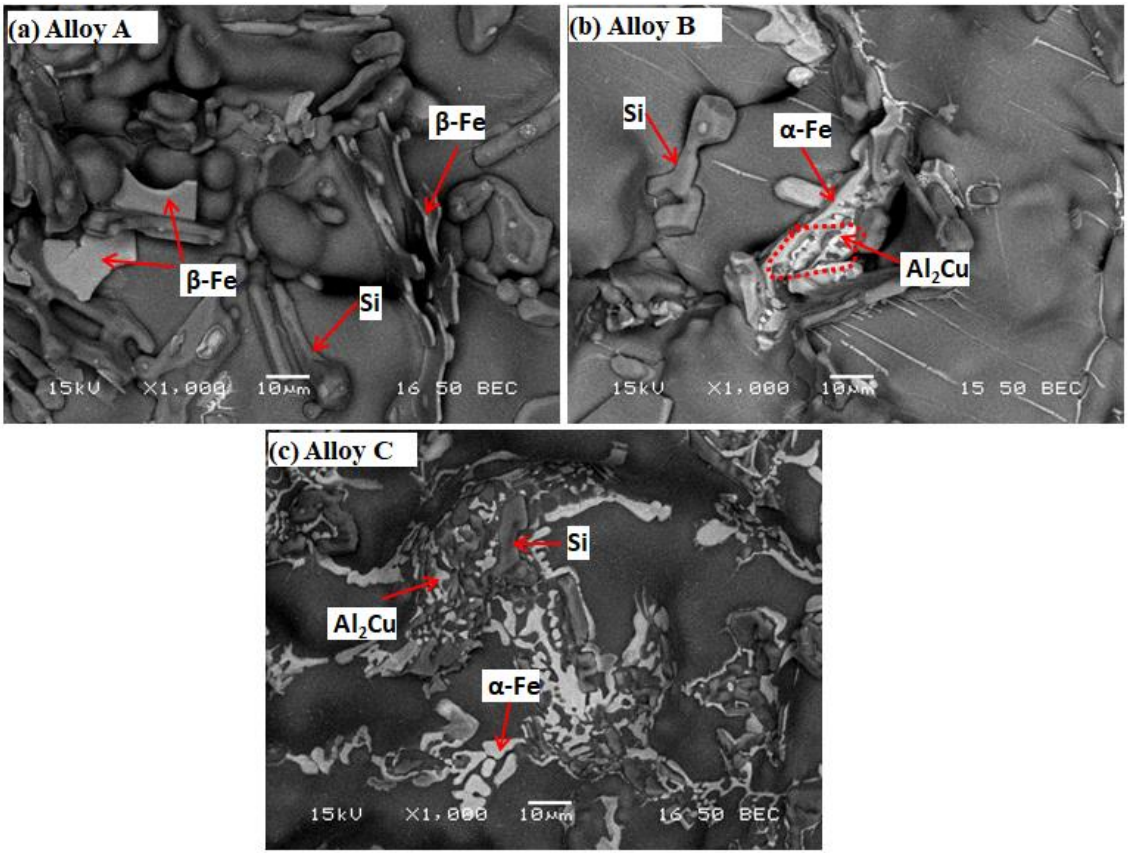

Fig. 11 Distribution of particles on the fracture after test at the liquid fraction of 3.35%

As shown in Fig. 11a, the platelet β-Fe and flake-like Si particles are on the fracture surface in Alloy A. They especially formed a wall-like structure due to the platelet morphology and then blocked the free flow of the low-meting liquid, leading to isolated liquid pockets in the interdendritic regions. Therefore, the crack can easily propagate along the path with platelets of β-Fe and flake-like Si particles with limited resistance to the fracture. However, due to the modification of the iron-bearing intermetallics from platelet β-Fe to Chinese script α-Fe in Alloy B (Fig. 11b), the partial low-meting liquid can flow through the branched α-Fe and feed the mushy zone before it is blocked, resulting in a higher strength and deformation before fracture [5, 10]. As indicated by the red circle in Fig. 11b, Al_2Cu is found to be associated with the branches of α-Fe. With the

combined additions of Mn and Sr in Alloy C, both the Si particles and iron-bearing intermetallics are finely branched (Fig. 3c), providing more paths for the low-meting liquid to pass through and promote liquid feeding due to the somewhat continuous liquid films in the interdendritic regions. As shown in Fig. 11c, intersected Si, α-Fe and Al_2Cu are observed in the fracture surface of Alloy C, confirming the possible liquid feeding. Therefore, Alloy C can accommodate a larger amount of deformation in the mushy zone before fracture with higher strength in compared with Alloys A and B.

4. Conclusions

In the present work, the high-temperature mechanical behavior near the solidus of Al-Si-Cu 319 cast alloys with the additions of Mn and Sr was studied with the following conclusions:

(1) The as-cast microstructure of 319 cast alloys is composed of eutectic Si particles, Al_2Cu and iron-bearing intermetallics. The dominant iron-bearing intermetallic was modified from platelet β-Fe to Chinese script α-Fe with the addition of Mn, while the flake-like eutectic Si was modified to fiber-like particles with the addition of Sr.

(2) High-temperature strength and ductility decreased with increasing test temperature in the solid state, attributed to the facilitated dislocation/grain boundary movement at higher temperatures. They both continued to decrease with increasing liquid fraction in the semisolid state due to the increased liquid portion surrounding the solid grains.

(3) The mechanical behavior at a given temperature near the solidus in 319 cast alloys is mainly controlled by two microstructural features: the iron-bearing intermetallics and eutectic Si particles. In both the solid and semisolid states, the modification from platelet β-Fe to Chinese script α-Fe intermetallic by the addition of Mn enhances the high-temperature mechanical properties. The simultaneous modification of the iron-bearing intermetallics and eutectic Si particles by the combined additions of Mn and Sr further improves the high-temperature mechanical properties.

(4) Based on the high-temperature strength and ductility near the solidus, the susceptibility to hot tearing decreases in the order of the base alloy, the Mn-containing

alloy with modified α-Fe intermetallic and then the Mn- and Sr-containing alloy with both modified α-Fe and eutectic Si.

Acknowledgments

The authors would like to acknowledge the financial support of the Natural Sciences and Engineering Research Council of Canada (NSERC) and Rio Tinto Aluminum through the NSERC Industry Research Chair in the Metallurgy of Aluminum Transformation at University of Quebec at Chicoutimi. Special thanks are given to Dr. A. Hekmat-Ardakan for his contribution in the experiments.

Conflicts of interest: The authors declare no conflict of interest.

References

[1] J.G. Kaufman, E.L. Rooy, Aluminum alloy castings : properties, processes, and applications, American Foundry Soc., Schaumburg, IL, 2007.
[2] C. Puncreobutr, P.D. Lee, K.M. Kareh, T. Connolley, J.L. Fife, A.B. Phillion, Influence of Fe-rich intermetallics on solidification defects in Al–Si–Cu alloys, Acta Mater. 68 (2014) 42-51.
[3] F. D'Elia, C. Ravindran, Influence of grain refinement on hot tearing in B206 and A319 aluminum alloys, T. Indian I. Metals 62(4) (2009) 315-319.
[4] G. Chen, J. Jiang, Z. Du, F. Han, H.V. Atkinson, Hot tensile behavior of an extruded Al–Zn–Mg–Cu alloy in the solid and in the semi-solid state, Mater. Des. 54 (2014) 1-5.
[5] A. Bolouri, K. Liu, X.-G. Chen, Effects of iron-rich intermetallics and grain structure on semisolid tensile properties of Al-Cu 206 cast alloys near solidus temperature, Metall. Mater. Trans. A 47(12) (2016) 6466-6480.
[6] E. Giraud, M. Suery, M. Coret, Mechanical Behavior of AA6061 Aluminum in the Semisolid State Obtained by Partial Melting and Partial Solidification, Metall. Mater. Trans. A 41(9) (2010) 2257-2268.
[7] S.M. Mohseni, A.B. Phillion, D.M. Maijer, Modelling the constitutive behaviour of aluminium alloy B206 in the as-cast and artificially aged states, Mater. Sci. Eng. A 649 (2016) 382-389.
[8] A. Alankar, M.A. Wells, Constitutive behavior of as-cast aluminum alloys AA3104, AA5182 and AA6111 at below solidus temperatures, Mater. Sci. Eng. A 527(29–30) (2010) 7812-7820.
[9] D.G. Eskin, Suyitno, L. Katgerman, Mechanical properties in the semi-solid state and hot tearing of aluminium alloys, Prog. Mater Sci. 49(5) (2004) 629-711.
[10] A.K. Dahle, T. Sumitomo, S. Instone, Relationship between tensile and shear strengths of the mushy zone in solidifying aluminum alloys, Metall. Mater. Trans. A 34(1) (2003) 105-113.
[11] G. Rajaram, S. Kumaran, T.S. Rao, High temperature tensile and wear behaviour of aluminum silicon alloy, Mater. Sci. Eng. A 528(1) (2010) 247-253.

[12] E. Rincón, H.F. López, M.M. Cisneros, H. Mancha, M.A. Cisneros, Effect of temperature on the tensile properties of an as-cast aluminum alloy A319, Mater. Sci. Eng. A 452–453 (2007) 682-687.
[13] A.B. Phillion, S. Thompson, S.L. Cockcroft, M.A. Wells, Tensile properties of as-cast aluminum alloys AA3104, AA6111 and CA31218 at above solidus temperatures, Mater. Sci. Eng. A 497(1–2) (2008) 388-394.
[14] L.J. Colley, M.A. Wells, D.M. Maijer, Tensile properties of as-cast aluminum alloy AA5182 close to the solidus temperature, Mater. Sci. Eng. A 386(1–2) (2004) 140-148.
[15] J.Z. Yi, Y.X. Gao, P.D. Lee, T.C. Lindley, Effect of Fe-content on fatigue crack initiation and propagation in a cast aluminum–silicon alloy (A356–T6), Mater. Sci. Eng. A 386(1–2) (2004) 396-407.
[16] Z. Ma, A.M. Samuel, F.H. Samuel, H.W. Doty, S. Valtierra, A study of tensile properties in Al–Si–Cu and Al–Si–Mg alloys: Effect of β-iron intermetallics and porosity, Mater. Sci. Eng. A 490(1–2) (2008) 36-51.
[17] J. Wang, M. Li, J. Allison, P.D. Lee, Multiscale modeling of the influence of Fe content in a Al–Si–Cu alloy on the size distribution of intermetallic phases and micropores, J. Appl. Phys. 107(6) (2010) 061804.
[18] C.M. Dinnis, J.A. Taylor, A.K. Dahle, Iron-related porosity in Al–Si–(Cu) foundry alloys, Mater. Sci. Eng. A 425(1–2) (2006) 286-296.
[19] N. Roy, A.M. Samuel, F.H. Samuel, Porosity formation in AI-9 Wt Pct Si-3 Wt Pct Cu alloy systems: Metallographic observations, Metall. Mater. Trans. A 27(2) (1996) 415-429.
[20] C.M. Dinnis, J.A. Taylor, A.K. Dahle, Interactions between iron, manganese, and the Al-Si eutectic in hypoeutectic Al-Si alloys, Metall. Mater. Trans. A 37(11) (2006) 3283-3291.
[21] S. Seifeddine, S. Johansson, I.L. Svensson, The influence of cooling rate and manganese content on the β-Al5FeSi phase formation and mechanical properties of Al–Si-based alloys, Mater. Sci. Eng. A 490(1–2) (2008) 385-390.
[22] K. Liu, X. Cao, X.G. Chen, Solidification of iron-rich intermetallic phases in Al-4.5Cu-0.3Fe cast alloy, Metall. Mater. Trans. A 42(7) (2011) 2004-2016.
[23] K. Liu, X. Cao, X.G. Chen, Tensile properties of Al-Cu 206 cast alloys with various iron contents, Metall. Mater. Trans. A 45(5) (2014) 2498-2507.
[24] S. Hegde, K.N. Prabhu, Modification of eutectic silicon in Al–Si alloys, J. Mater. Sci. 43(9) (2008) 3009-3027.
[25] M. Zamani, S. Seifeddine, M. Aziziderouei, The Role of Sr on Microstructure Formation and Mechanical Properties of Al-Si-Cu-Mg Cast Alloy, in: B.A. Sadler (Ed.) TMS-Light metals 2013, John Wiley & Sons, Hoboken, NJ, USA, 2013.
[26] H. Qiu, H. Yan, Z. Hu, Modification of near-eutectic Al–Si alloys with rare earth element samarium, J. Mater. Res. 29(11) (2014) 1270-1277.
[27] J.H. Li, X.D. Wang, T.H. Ludwig, Y. Tsunekawa, L. Arnberg, J.Z. Jiang, P. Schumacher, Modification of eutectic Si in Al–Si alloys with Eu addition, Acta Mater. 84 (2015) 153-163.
[28] Y. Birol, Solid fraction analysis with DSC in semi-solid metal processing, J. Alloys Compd. 486(1–2) (2009) 173-177.

[29] A.M.A. Mohamed, F.H. Samuel, S.A. kahtani, Microstructure, tensile properties and fracture behavior of high temperature Al-Si-Mg-Cu cast alloys, Mater. Sci. Eng. A 577 (2013) 64-72.
[30] E. Rincon, H.F. Lopez, M.M. Cisneros, H. Mancha, Temperature effects on the tensile properties of cast and heat treated aluminum alloy A319, Mater. Sci. Eng. A 519(1-2) (2009) 128-140.
[31] A. Garza-Delgado, K. Kabiri-Bamoradian, R.A. Miller, Determination of elevated-temperature mechanical properties of an aluminum A380.0 die casting alloy in the as-cast condition, Die Cast. Eng. 52(6) (2008) 40-46.
[32] R.K. Mahidhara, A.K. Mukherjee, High temperature flow and failure processes in an Al-13 wt % Si eutectic alloy, J. Mater. Sci. 32(3) (1997) 809-814.
[33] M. Zamani, S. Seifeddine, A.E.W. Jarfors, High temperature tensile deformation behavior and failure mechanisms of an Al–Si–Cu–Mg cast alloy — The microstructural scale effect, Mater. Des. 86 (2015) 361-370.
[34] F. Mao, G. Yan, Z. Xuan, Z. Cao, T. Wang, Effect of Eu addition on the microstructures and mechanical properties of A356 aluminum alloys, J. Alloys Compd. 650 (2015) 896-906.
[35] H. Kamguo Kamga, D. Larouche, M. Bournane, A. Rahem, Hot tearing of aluminum–copper B206 alloys with iron and silicon additions, Mater. Sci. Eng., A 527(27) (2010) 7413-7423.
[36] L. Sweet, M.A. Easton, J.A. Taylor, J.F. Grandfield, C.J. Davidson, L. Lu, M.J. Couper, D.H. StJohn, Hot Tear Susceptibility of Al-Mg-Si-Fe Alloys with Varying Iron Contents, Metall. Mater. Trans. A 44(12) (2013) 5396-5407.
[37] A. Bjurenstedt, S. Seifeddine, A. Jarfors, The Effects of Fe-Particles on the Tensile Properties of Al-Si-Cu Alloys, Metals 6(12) (2016) 314.